Supporting Information

Magneto-electrochemistry driven ultralong-life Zn-VS_2 aqueous zinc-ion batteries

Yunjie Mao,[ab] Jin Bai, *[a] Jianguo Si,*[c] Hongyang Ma,[ab] Wanyun Li,[ab] Peiyao Wang,[ab] Hongli Zhang,[d] Zhigao Sheng,[e] Xiaoguang Zhu,[a] Peng Tong,[a] Xuebin Zhu,[a] Bangchuan Zhao*[a] and Yuping Sun[ae]

[a]Key Laboratory of Materials Physics, Institute of Solid State Physics, HFIPS, Chines e Academy of Sciences, Hefei 230031, People's Republic of China

[b] University of Science and Technology of China, Hefei 230026, People's Republic of China

[c] Spallation Neutron Source Science Center, Institute of High Energy Physics, Chinese Academy of Sciences, Dongguan 523803, People's Republic of China

[d] Gotion High-tech Co., Ltd., Hefei 230051, People's Republic of China

[e] High Magnetic Field Laboratory, Chinese Academy of Sciences, Hefei 230031, People's Republic of China

*Corresponding Authors, E-mail: jbai@issp.ac.cn; sijg@ihep.ac.cn; bchzhao@issp.ac.cn

Experimental Section

Synthesis of VS_2 nanosheets.

The pristine accordion-like VS_2 nanosheets were prepared by a facile one-step hydrothermal synthesis method. In first, 2 mmol NH_4VO_3 and 15 mmol thioacetamide (TAA) were added in 30 ml deionized water containing 2 ml $NH_3{\bullet}H_2O$ as the V and S sources with continuous stirring for 60 min. Then the above mixture was poured into a 50 ml autoclave and kept in a furnace at 180 °C for 10 h. After cooling down to room temperature naturally and the products were washed with ethanol and deionized water for several times. Finally, the powder was dried at 60 °C in a vacuum oven overnight.

Characterizations

The scanning electron microscope (SEM), transmission electron microscope (TEM) and high-resolution transmission electron microscope (HRTEM) characterizations were employed to obtain material morphology, crystallization, and microstructure information of the materials. And the elemental mapping analysis of the materials was carried out in energy dispersive spectroscopy (EDS) attached to SEM and TEM. The structure and phase purity of the materials was characterized by X-ray diffraction (XRD) with Cu Kα radiation. Raman spectroscopy measurment was performed on the Horiba Jobin Yvon T6400 equipment with 514.5 nm laser excitation. X-ray photoelectron spectra (XPS) was measured using a Thermo Scientific ESCALAB 250 with Al Kα as the excitation source. Electron spin resonance (ESR) signal was collected by the Bruker EMX plus equipment.

Electrochemical measurements

The electrochemical tests were carried out in coin-type cell (CR2032) including VS_2 as cathode, glass fiber (GF/D) as separator, metallic zinc slice as anode, and 4 M $Zn(CF_3SO_3)_2$ as electrolyte. To prepare cathode, the VS_2 active materials, Super P conductive agent and Poly(vinylidene difluoride) (PVDF) binder were firstly mixed in a weight ratio of 7:2:1 in N-methyl-2-pyrrolidone (NMP) solvent. And then the slurry was brush-coated onto stainless steel mesh (SS) and dried in vacuum at 70 °C for 12 h. The loading mass of the active material is about 2 mg cm^{-2}. The CV tests at a scan rate of 0.2-1.0 mV s^{-1} were performed on an electrochemical workstation (CHI660E). Galvanostatic charge/discharge (GCD) and galvanostatic intermittent titration technique (GITT) processes were conducted by the LAND CT2001A device. The symmetric cells with a glass fiber filter and 4 M $Zn(CF_3SO_3)_2$ aqueous electrolyte solution were fabricated using Zn slices with a diameter of 16 mm as both the working

and counter electrodes. The voltage profiles of the symmetric cells were measured at a current density of 0.5 mA cm^{-2} with a constant areal capacity of 0.5 mAh cm^{-2}. The galvanostatic intermittent titration technique (CE) of Zn plating/stripping was estimated using a Cu||Zn half-cell, which was operated at a current density of 0.5 mA cm^{-2} for 0.5 h during Zn plating on the Cu foil, and performed at the same current density until 1.0 V (*vs.* Zn/Zn^{2+}) during stripping of the plated Zn on the Cu foil. Cycling performance was tested by LAND battery test system under a simple NdFeB permanent magnet with a magnetic field of about 4000 Oe.

Computational methods

The first-principles calculations based on density function theory (DFT) were performed by the Vienna Ab-initio Simulation Package (VASP). The projector-augmented wave (PAW) pseudopotential with Perdew-Burke-Ernzerhof (PBE) parametrization according to the generalized gradient approximation (GGA) were used to treat the interaction between the valance electrons and ionic cores. The on-site Coulombic interaction of V 3*d*-electrons were treated by the DFT+U method, where the effective Hubbard U was set as 3.25 eV. The DFT-D3 correction method was used to describe the van der Waals interaction. The cut-off energy for the wave function is set as 500 eV, and the Brillouin zone was sampled via Monkhorst-Pack scheme with a $0.02 \times 2\pi Å^{-1}$ space. The intercalation energy of Zn inserted into the VS_2 or VS_4 framework was calculated by $E_B=E_{Zn@VSx}-(E_{Zn}+E_{VSx})$, where the $E_{Zn@VSx}$, E_{Zn}, E_{VSx} are the energy of Zn-inserted VS_2 (VS_4), isolated Zn atom and VS_2 (VS_4) framework. The charge transfer was evaluated by Bader charge analysis.

Simulation methods

To elucidate the inhibition effect of the magnetic field in Zn dendrite growth, a simplified 3D electric field distribution and the trajectory of zinc ions with or without magnetic field model based on COMSOL Multiphysics 5.6 software were established. The magnetic field was settled at 4000 Oe and 4 tiny protrusion is suggested to exist on the surface of the 50 μm Zn metal.

Supporting Figures and discussions

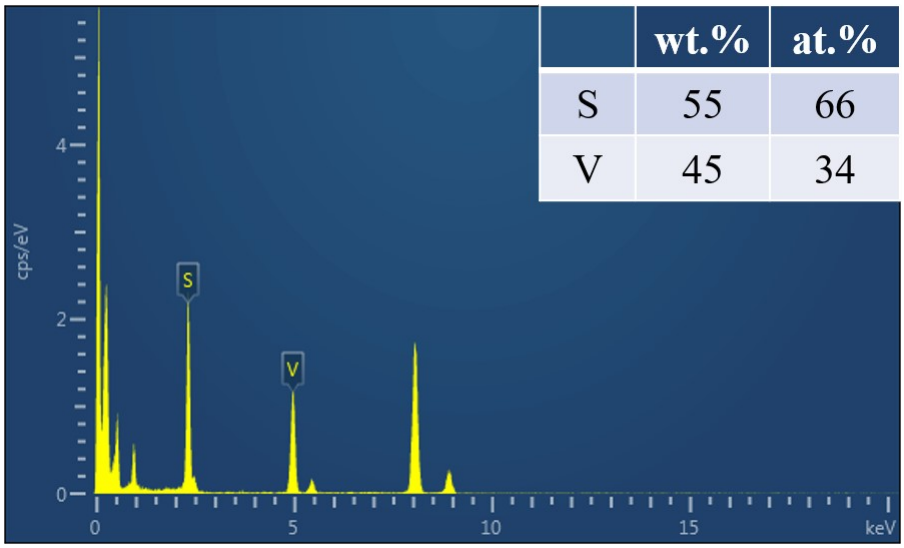

	wt.%	at.%
S	55	66
V	45	34

Fig. S1. The weight and atomic ratio of V and S in the pristine VS_2.

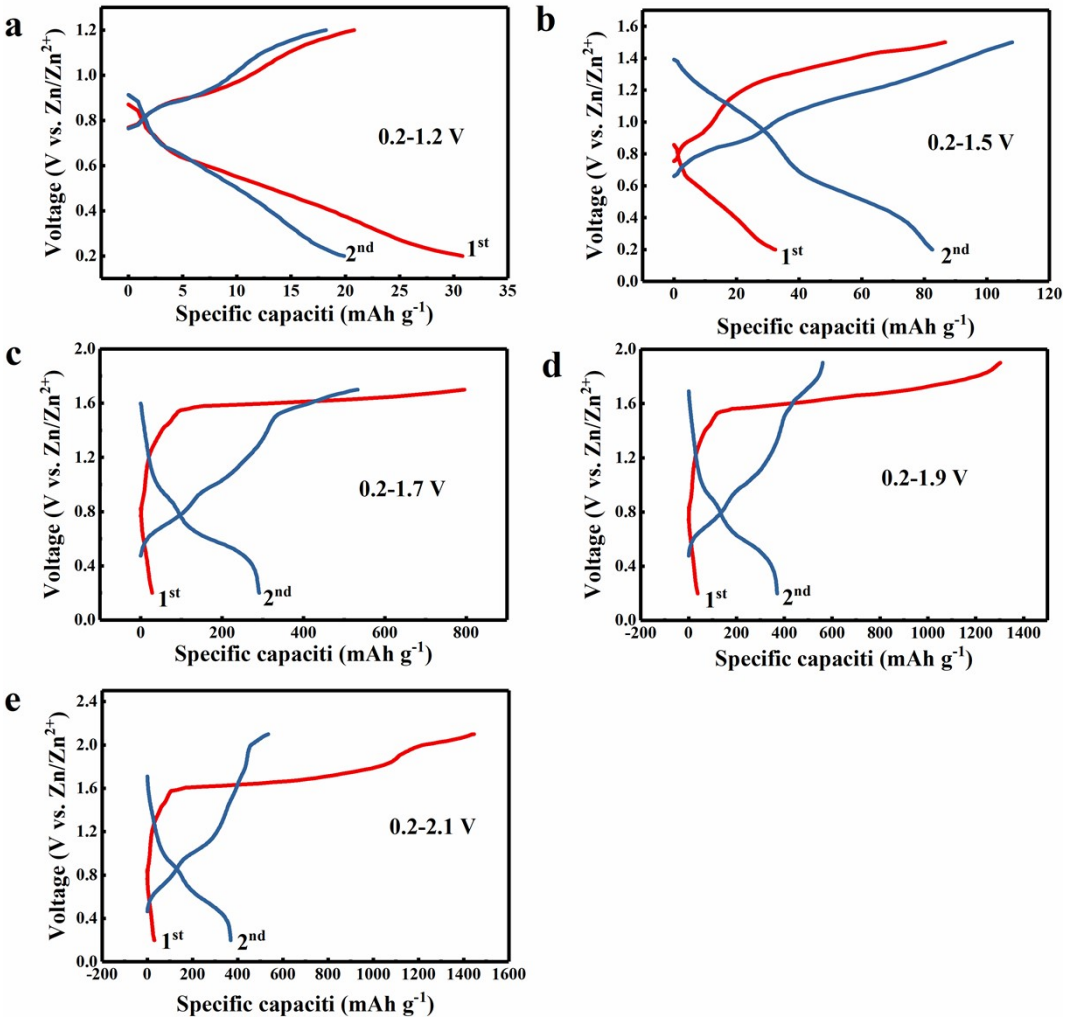

Fig. S2. First two cycles GCD curves for VS_2 cathode at different charge cut-off voltages. (a-e) The charge cut-off voltage at 1.2 V (a), 1.5 V(b), 1.7 V (c), 1.9 V (d) and 2.1 V(e).

As shown in Fig. S2, benefited from the "water in salt" features of the high concentration electrolyte, the assembled battery could smoothly cycle even under much higher voltage, which could effectively avoid the decomposition of water and the occurrence of serious side reactions. When the charge cut-off voltage is lower, the intercalation/deintercalation of Zn^{2+} is limited, while more side reactions will happen when the charge cut-off voltage is higher.

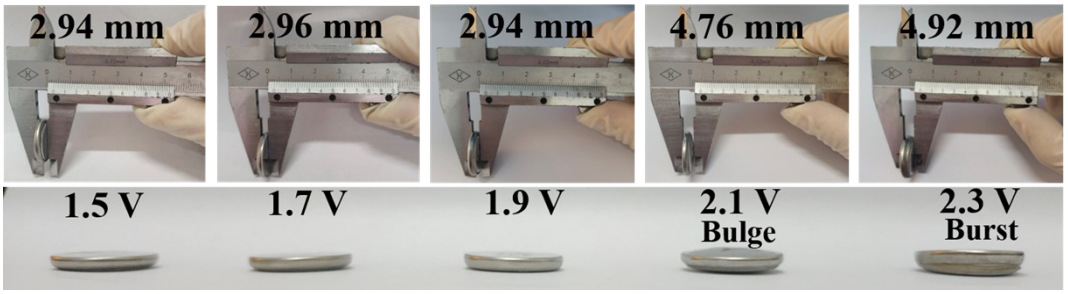

Fig. S3. Optical photos of the thickness of VS_2||Zn batteries at different charge cut-off voltages.

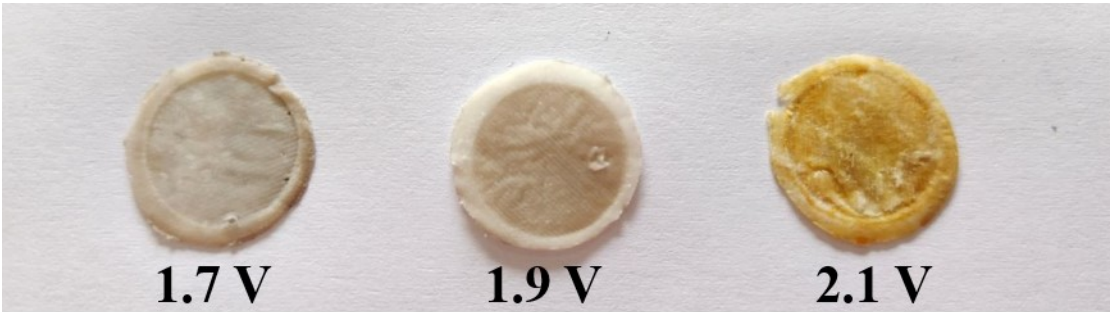

Fig. S4. Optical photos of the fiberglass separators at different charge cut-off voltages.

Fig. S3 and Fig. S4 show the situation of the battery and separator under different charge cut-off voltages, and it can be seen that the batteries and the separators have almost no change when the charge cut-off voltage is ≤ 1.9 V. When the charge cut-off voltage is ≥ 2.1 V, the batteries bulged and burst, and the separator turned yellow, which is caused by the serious side reactions with gas production due to the fact that the electrolyte cannot withstand much higher voltage of ≥ 2.1 V.

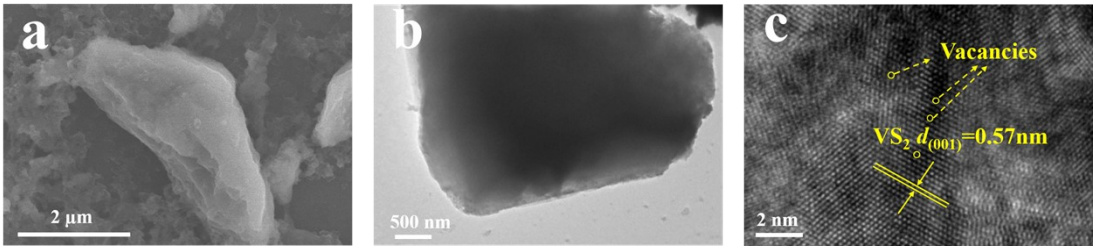

Fig. S5. Morphology and lattice characterization of the VS_2 cathode at the charge cut-off voltage of 1.7 V. (a-c) SEM(a), TEM(b) and HRTEM images (c) of the VS_2 cathode.

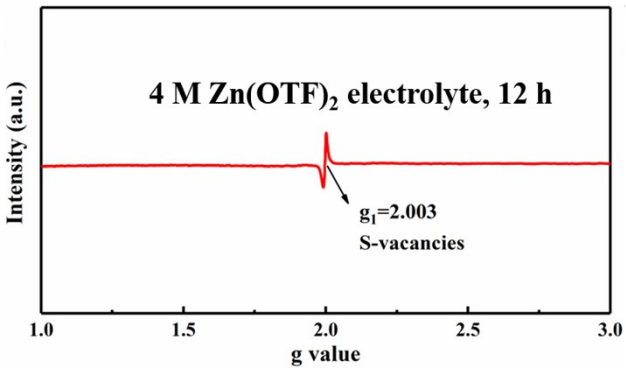

Fig. S6. The ESR spectrum of the orignal VS_2 electrode soaked in the electrolyte of 4 M $Zn(OTf)_2$ for 12 h.

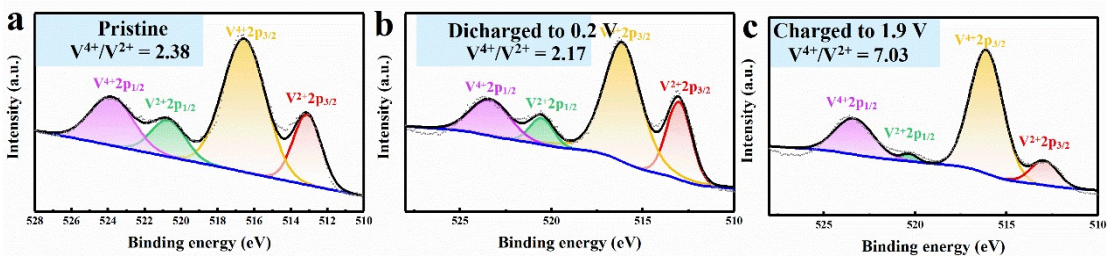

Fig. S7. The XPS characterizations of VS_2. The high-resolution V 2p XPS of (a) pristine cathode, (b) discharged to 0.2 V and (c) charged to 1.9 V.

Fig. S7 show that the ratios of V^{4+}/V^{2+} are about 2.38 and 2.17 for the pristine and zinc ions intercalated VS_2, which has no obvious change for the two materials. It is worth noting that the peak of the V^{2+} becomes extremely weak after full charged and the ratio of V^{4+}/V^{2+} changed to about 7.03, indicating that the unstable V^{2+} tends to change into the more stable V^{4+} and along with the escape of few vanadium atoms under the condition of high system energy in the process of high voltage charging process, which is consistent with the *ex situ* XRD results.

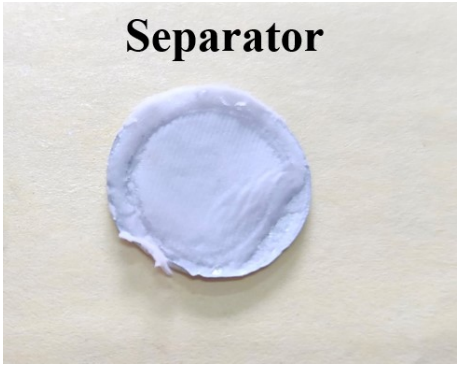

Fig. S8. The optical photograph of the separator for the disassembled battery without VS_2 coating after 100 cycles.

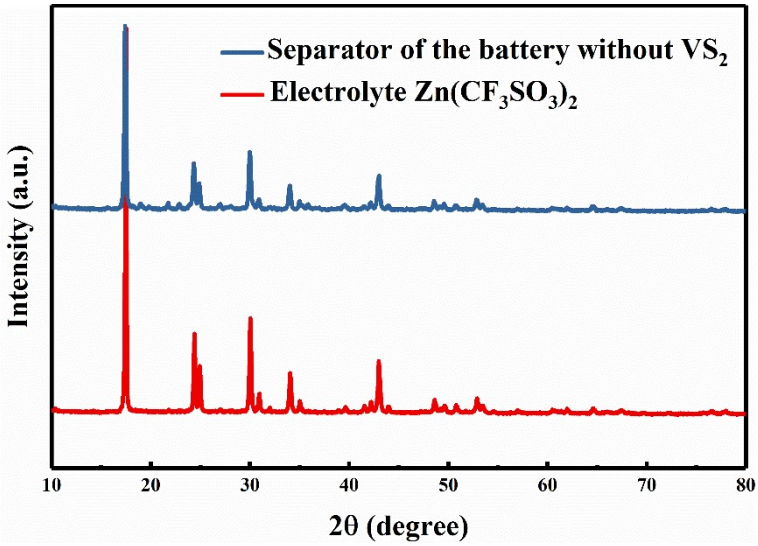

Fig. S9. The XRD patterns of the separator from the battery without VS_2 coating and $Zn(CF_3SO_3)_2$.

The similar discharge and charge measurements were also performed on a blank stainless-steel mesh without VS_2 coating to define the reaction pathway. After 100 cycles, the battery was disassembled and the separator was separatord from the battery as shown in Fig. S8. The separator in the battery without VS_2 coating almost kept its original shape and color. We carried out the XRD characterization of the separator after dried it in vacuum and the result is shown in Fig. S9. It can be seen that all diffraction peaks in the Fig. can be accurately indexed to the $Zn(CF_3SO_3)_2$ electrolyte, and no any impurity phases can be detected in the XRD pattern, indicating that the electrolyte was not oxidized at high cut-off voltage.

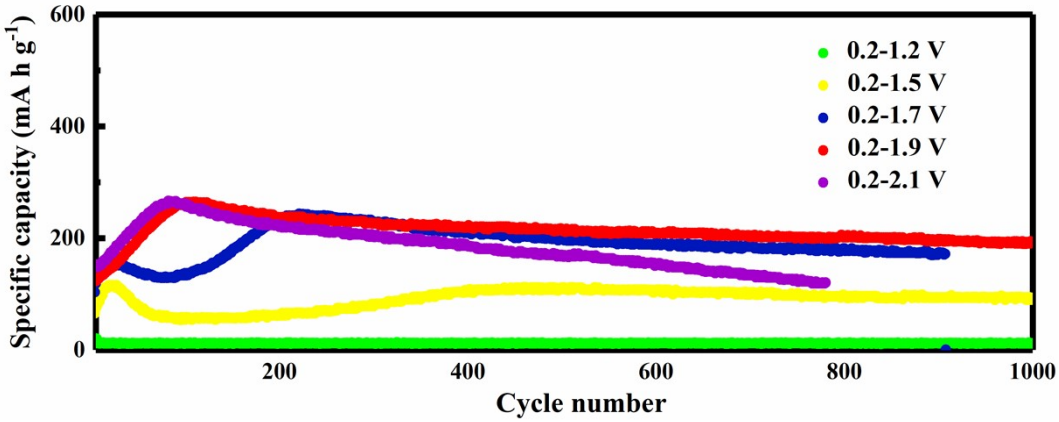

Fig. S10. The cycle performance at 5 A g^{-1} of the VS_2 cathode under different voltage windows.

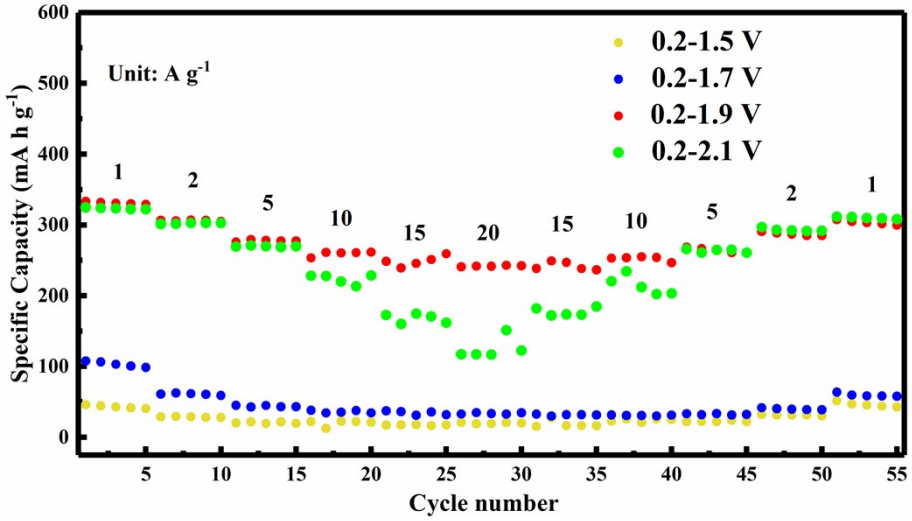

Fig. S11. The rate performance of the VS_2 cathode under different voltage windows.

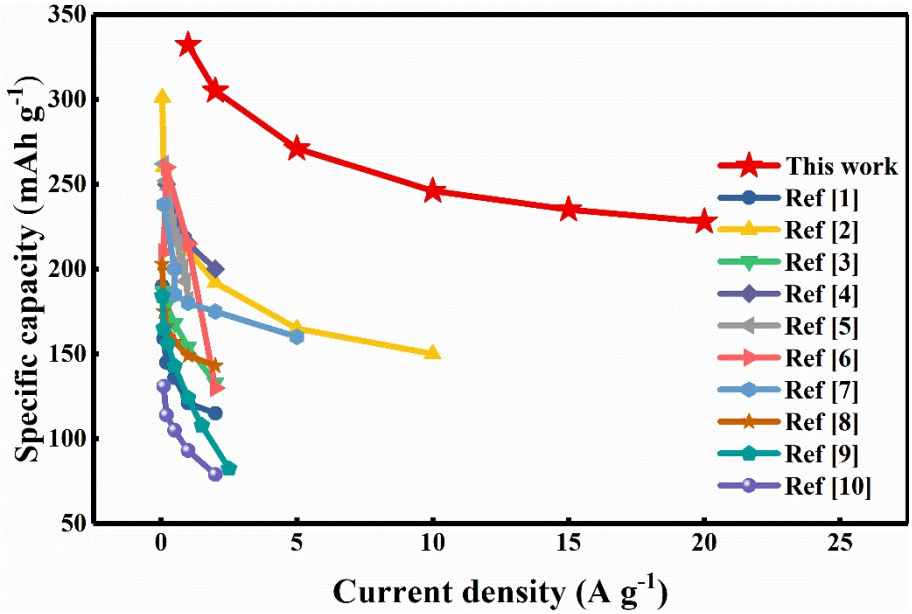

Fig. S12. The rate performance comparation between VS_2 and similar structure cathodes in AZIBs.

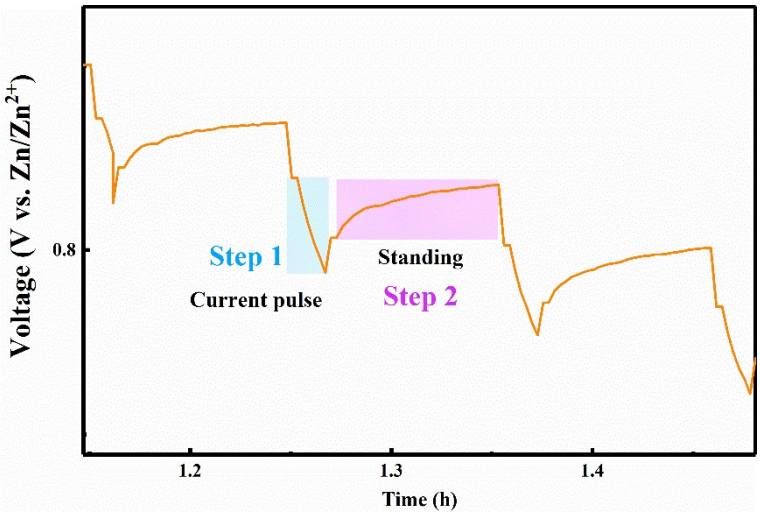

Fig. S13. Selected steps of the GITT curves during discharge process.

As shown in Fig. S13, in the step 1: a constant amount of zinc ions is adsorbed into the VS_2 cathode surface during each current pulse due to the constant pulse current and time interval. In this process, zinc ions will diffusion from the solution to the surface of the material. Step 2: Then turn off the pulse current and let the battery stand for a period of times. Driven by the ionic concentration gradient and chemical potential, zinc ions will diffuse from the cathode surface to the inside of the material (that is from the cathode surface to the bulk diffusion), resulting into the decrease of the concentration of zinc ions on the VS_2 cathode surface, and then the rise of the working voltage.

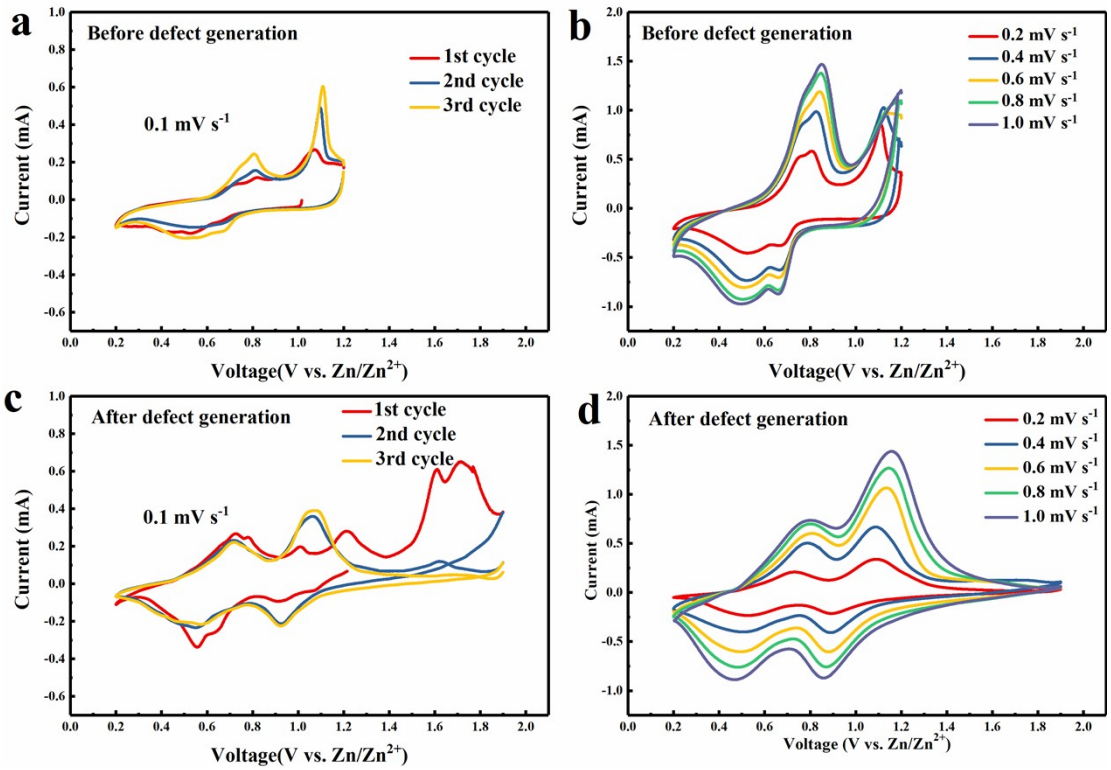

Fig. S14. The CV curves of the VS_2 cathode before and after defect generation. (a, c) The first three cycles CV curves at 0.1 mV s^{-1} of the VS_2 cathode before and after defect generation. (b, d) The CV curves at different scan rate of the VS_2 cathode before and after defect generation.

The CV curves before and after defect generation in VS_2 at the different scanning rates of 0.1-1.0 mV s^{-1} were supplied as shown in Fig. S14, and it can be seen that the integrated area of the CV curves before the defect generation is greatly smaller than that of after the generation of defects at the same scanning rate, indicating that the VS_2 shows a stronger zinc storage capability after the generation of V vacancy defects.

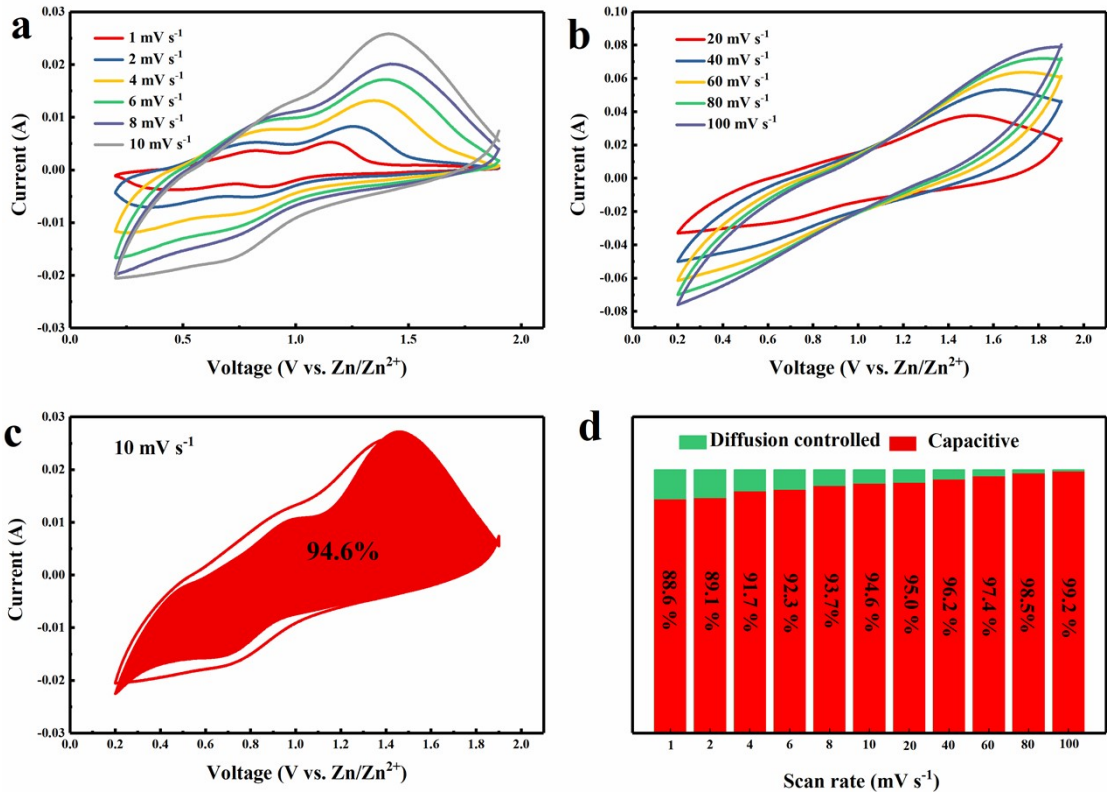

Fig. S15. (a, b) The CV curves of VS_2 at various scan rate from 1 to 100 mV s^{-1}. (c) Capacitive contribution fitting at 10 mV s^{-1}. (d) The contribution ratio of the capacitive and diffusion-controlled currents.

The CV curves at series scan rates from 1 to 100 mV s^{-1} were provide as shown in Fig. S15. It can be seen that the redox peak becomes broader as the scanning rate increases and almost disappeared when the scanning rate reaches 10.0 mV s^{-1}, indicating that the zinc storage process of VS_2 cathode is mainly controlled by pseudocapacitance process at the high scan rates. A typical fitting curve at the high scan rate of 10 mV s^{-1} is shown in Fig. S15c in this response letter, and nearly 94.6% of the total capacity is contributed by the capacitive process. And the calculation results of pseudocapacitance contribution at the different scan rates (1-100 mV s^{-1}) are shown in Fig. S15d. The pseudocapacitive contribution gradually increases with the increasing scan rate and reaches a highest value of 99.2% at the scan rate of 100 mV s^{-1}.

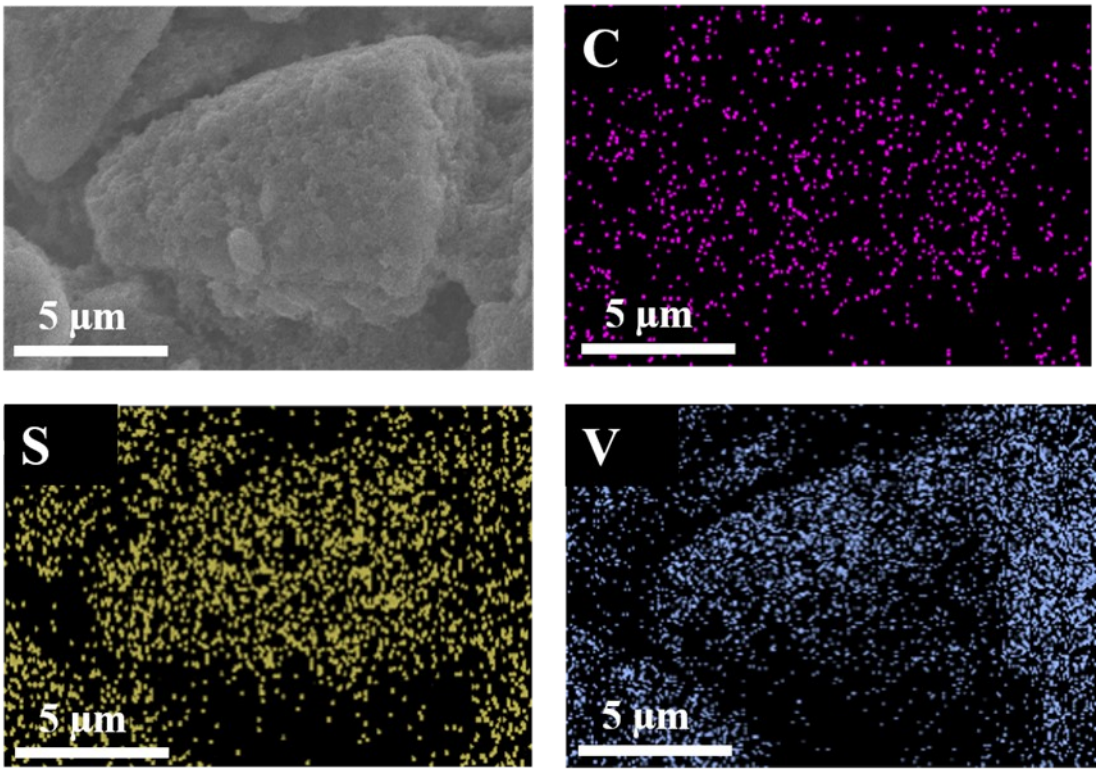

Fig. S16. The EDS mapping images of the VS_2 cathode at the charged state of 1.9 V.

As shown in Fig. S16, when VS_2 is charged to 1.9 V, the uniform distribution of V and S elements is basically maintained. The presence of C element in Fig. S16 is caused by the addition of Super P during cathode preparation.

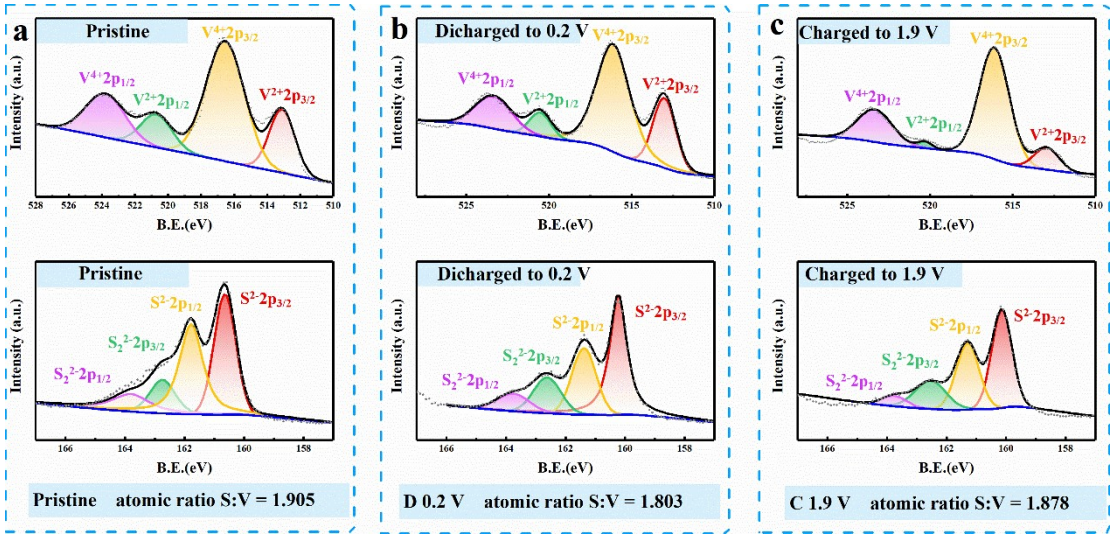

Fig. S17. The high-resolution V 2p and S 2p XPS spectra at different charge and discharge states in the VS_2 cathode. (a) Pristine state. (b) Discharged state of 0.2 V. (c) Charged state of 1.9 V.

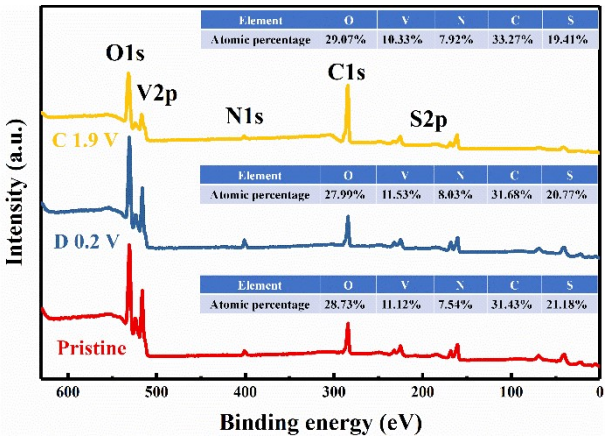

Fig. S18. The XPS survey spetra and atomic percentage in the VS_2 cathode at the different discharge and charge states.

The *ex situ* XPS result of the VS_2 cathode materials at different discharge and charge states was supplied as shown in Fig. S17. The atomic ratio of V/S is about 1.905 at the pristine state (Fig. S17a), and it changed to 1.803 at the discharged state of 0.2 V (Fig. S17b), indicating the formation of the sulfur vacancies. Moreover, the atomic ratio of V/S changed to 1.878 as charged to 1.9 V (Fig. S17c), indicating the formation of the vanadium vacancies. The *ex situ* XPS results is consistent with the *ex situ* ESR results in the original manuscript. It's worth noting that the valence state of V is mainly +4 at the charged state of 1.9 V and the signal of V^{2+} becomes very weak in the *ex situ* XPS spectrum, indicating that the formation of vanadium vacancy was due to the escape of V^{2+} during the high-voltage charging process. As shown in Fig. S18, the atomic

percentage change of oxygen is so small that it can be almost ignored, indicating that no oxygen released in the high-voltage charging process, which is consistent with the *ex situ* XRD result.

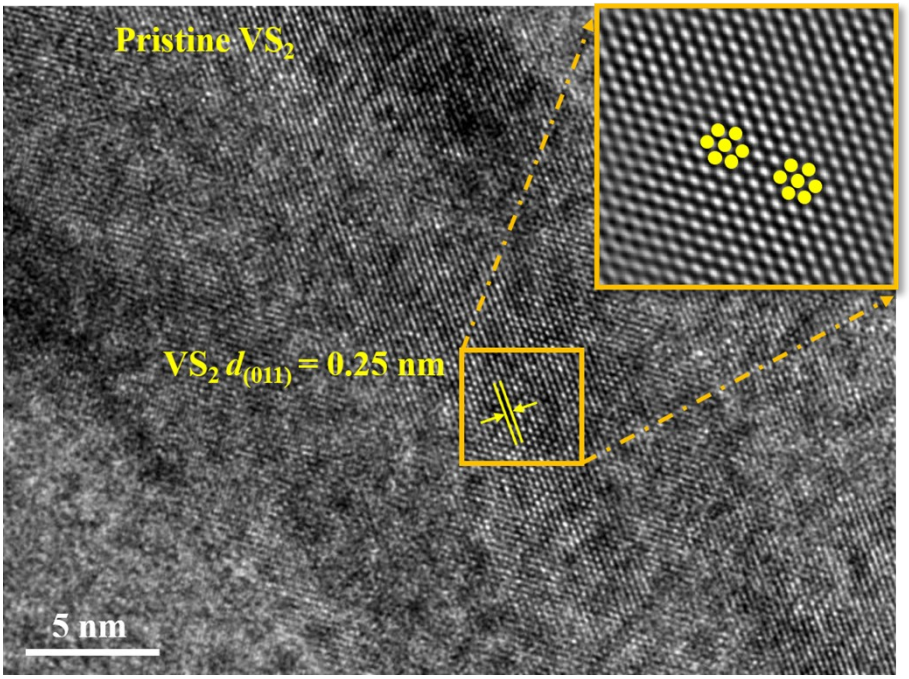

Fig. S19. The HRTEM image of the pristine VS_2.

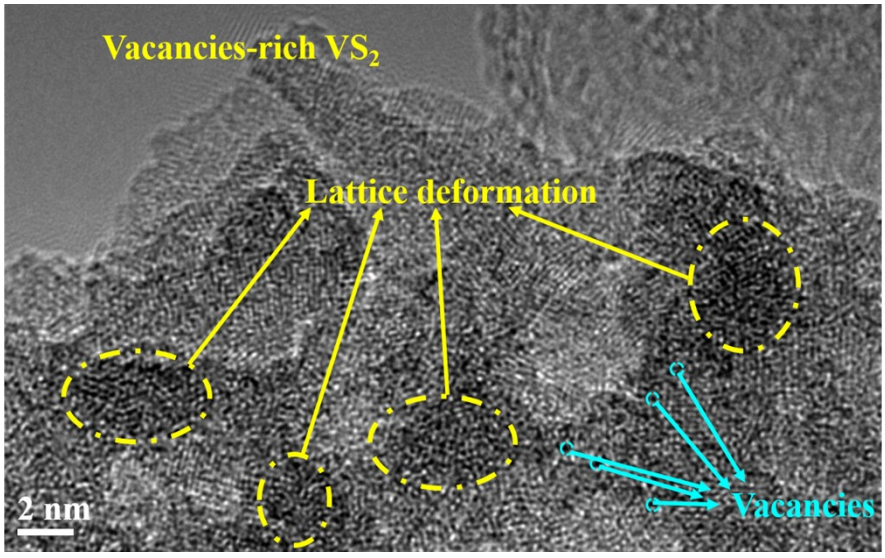

Fig. S20. The HRTEM image of the vacancies-rich VS_2 at the 1.9 V charged state in the first cycle.

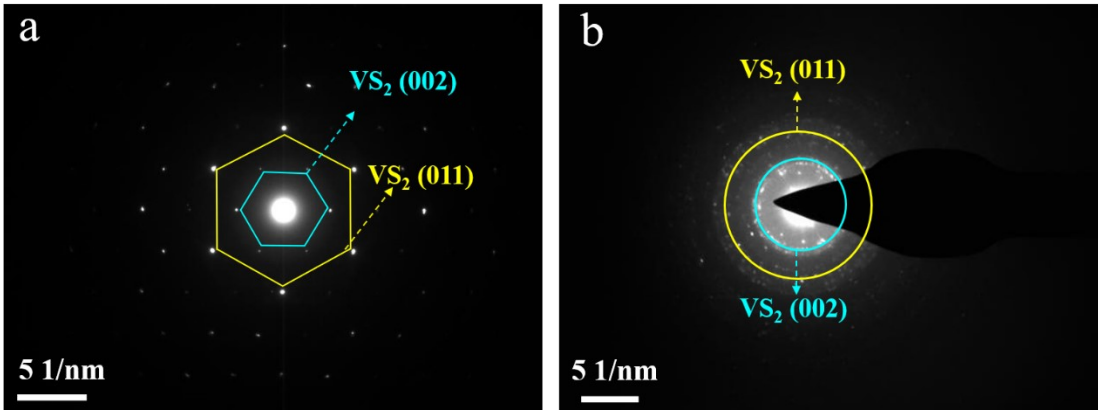

Fig. S21. SAED images of VS_2. (a) At the pristine state. (b) At the charged state of 1.9 V in the first cycle.

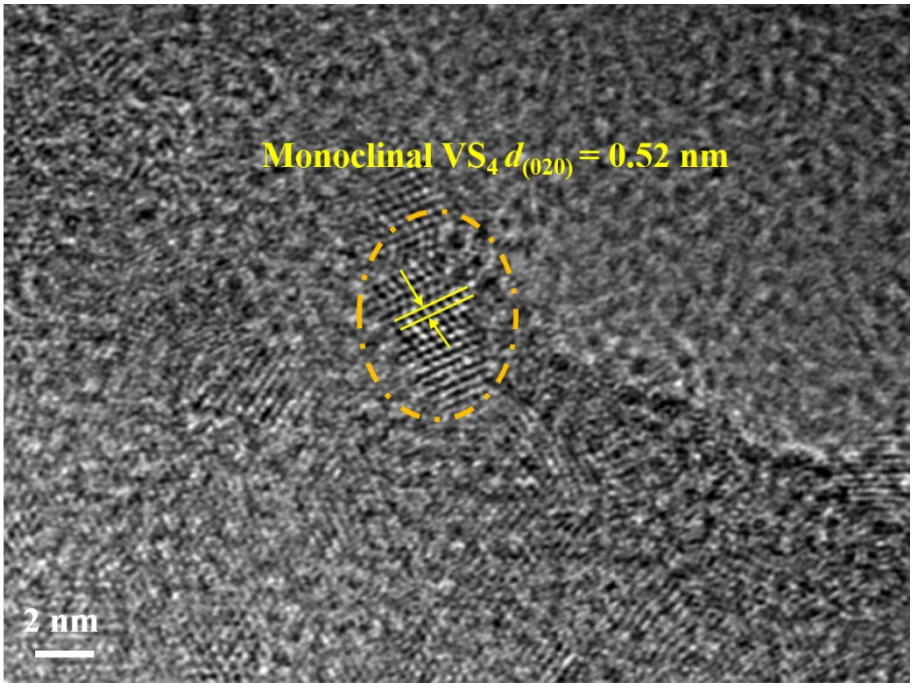

Fig. S22. The HRTEM image of the monoclinal VS_4 in the 0.2 V discharged state of second cycle.

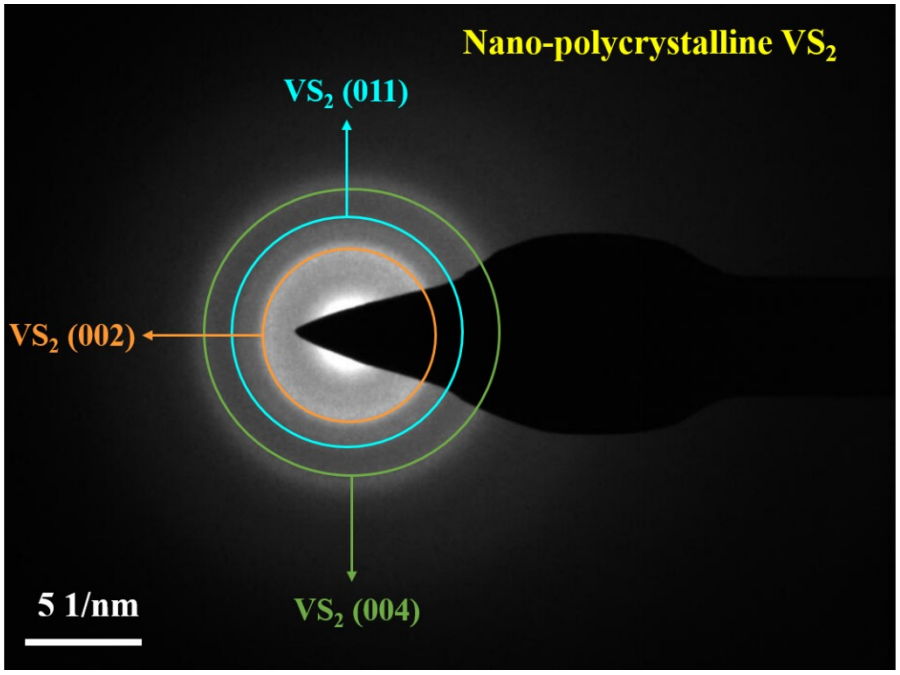

Fig. S23. The SAED image of the nano-polycrystalline VS_2 in the 1.9 V charged state of the second cycle.

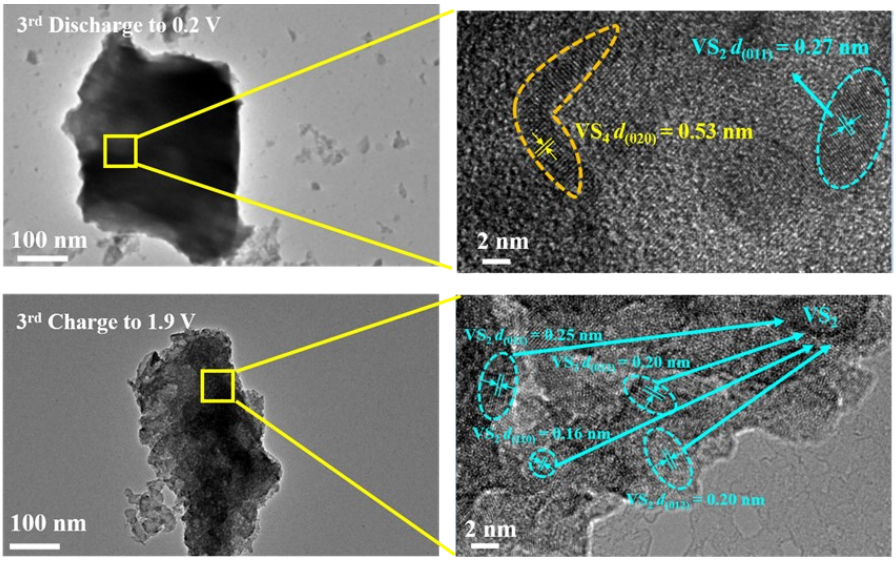

Fig. S24. *Ex situ* TEM and HRTEM images of the vacancies-rich VS_2 cathode in the third cycle.

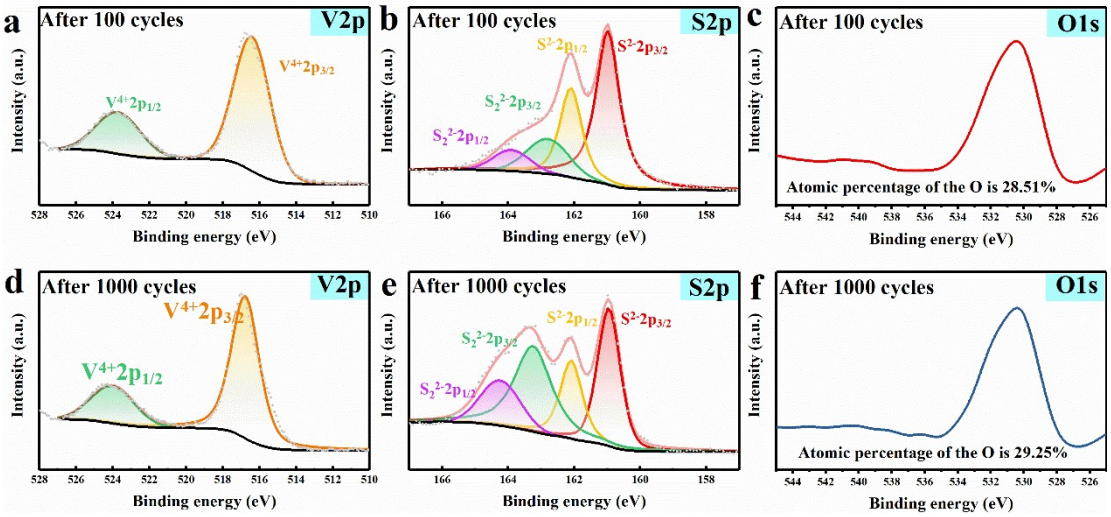

Fig. S25. The high-resolution V 2p, S 2p and O 1s XPS spectraof the VS_2 cathode after 100 (a-c) and 1000 cycles (d-f).

The XPS characterization of the VS_2 cathode material after 100 and 1000 cycles were carried out as shown in Fig. S25. It can be seen that the valence state of V is +4 and the peak of V^{2+} almost disappear, indicating the formation of V vacancy during the first few cycles high cut-off voltage charging process. And the enhanced XPS peak of S_2^{2-} after 1000 cycles is an indication of the presence of VS_4 phase during the discharging process. The atomic percentage of O element has almost no change at the different cycles, which indicates that again the oxygen may not be an intrinsic component of the sample and does not participate in the electrochemical reaction process.

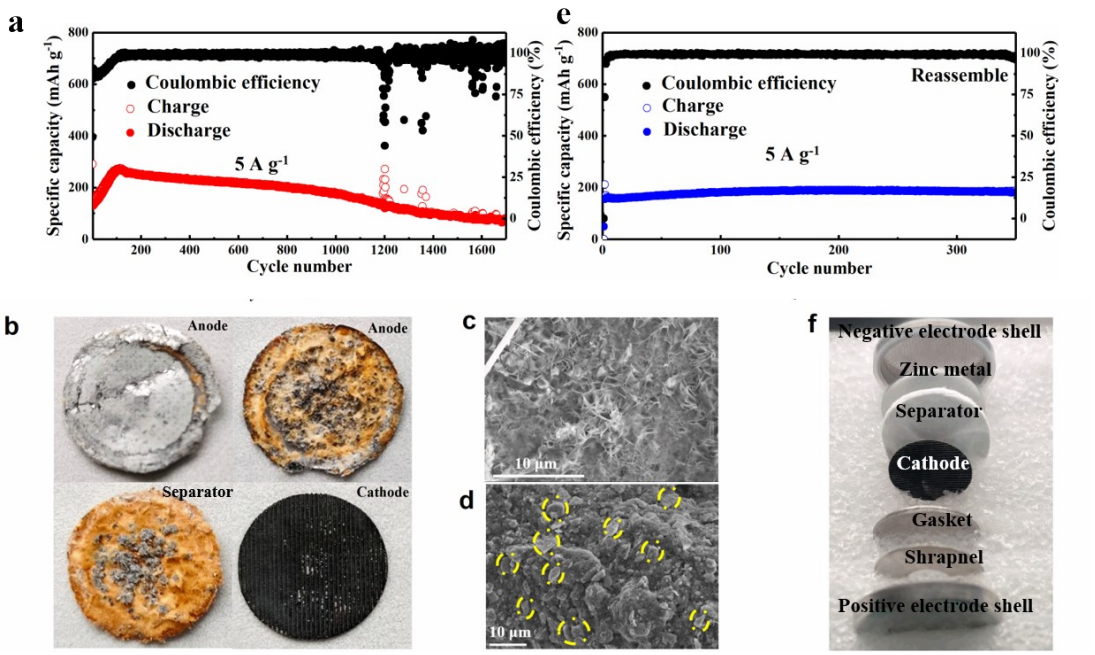

Fig. S26. Indirect analysis of the unsatisfactory cyclic stability. (a) The cycle performance of the VS_2 cathode. (b) The optical photos of the cathode, anode and separator after 1,700 cycles. (c) SEM image of the zinc metal anode after 1,700 cycles. (d) SEM image of the VS_2 cathode after 1,700 cycles. (e) Cycling performance of reassembled battery used the cathode in Fig. S16b. (f) The optical photos of the reassembled battery.

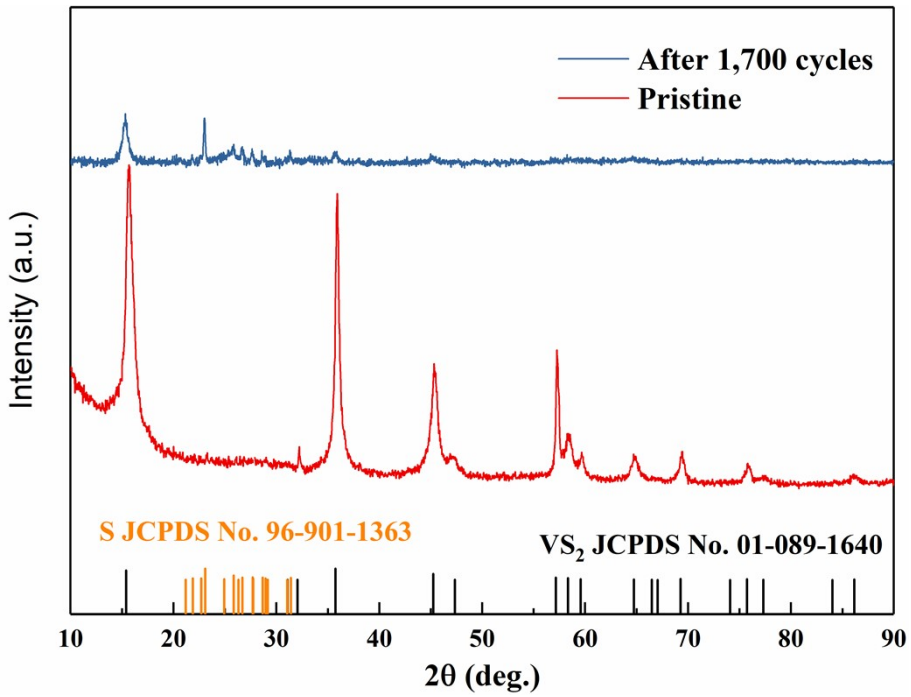

Fig. S27. The XRD patterns of the VS_2 cathode at the different cycling states.

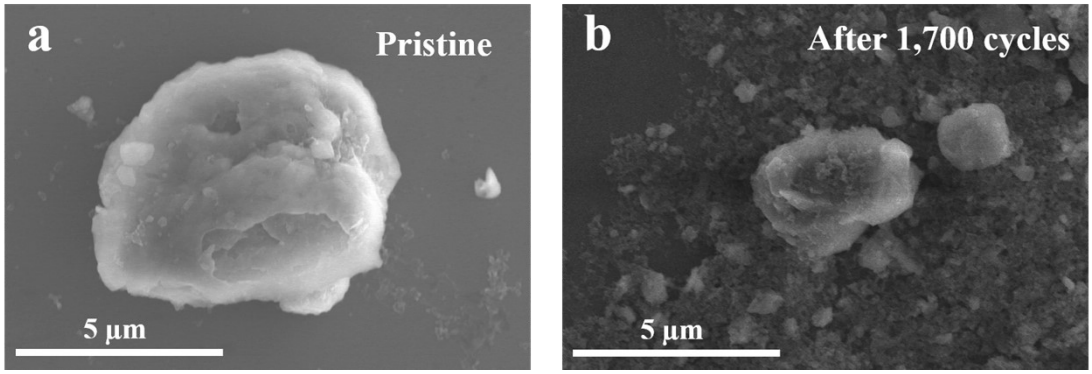

Fig. S28. The SEM images of the VS_2 cathode at the different cycling states.

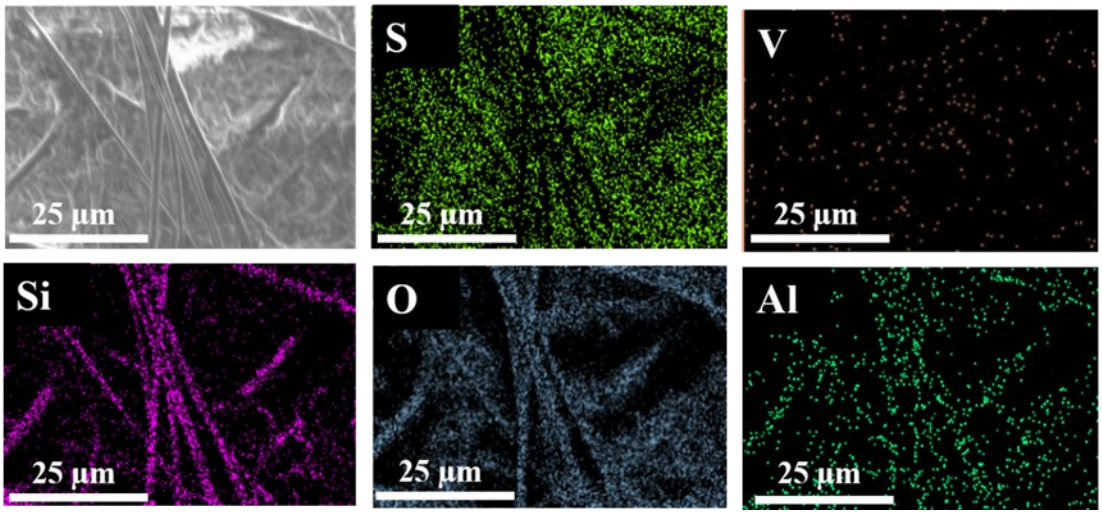

Fig. S29. The EDS mapping images of the yellow separator after 300 cycles.

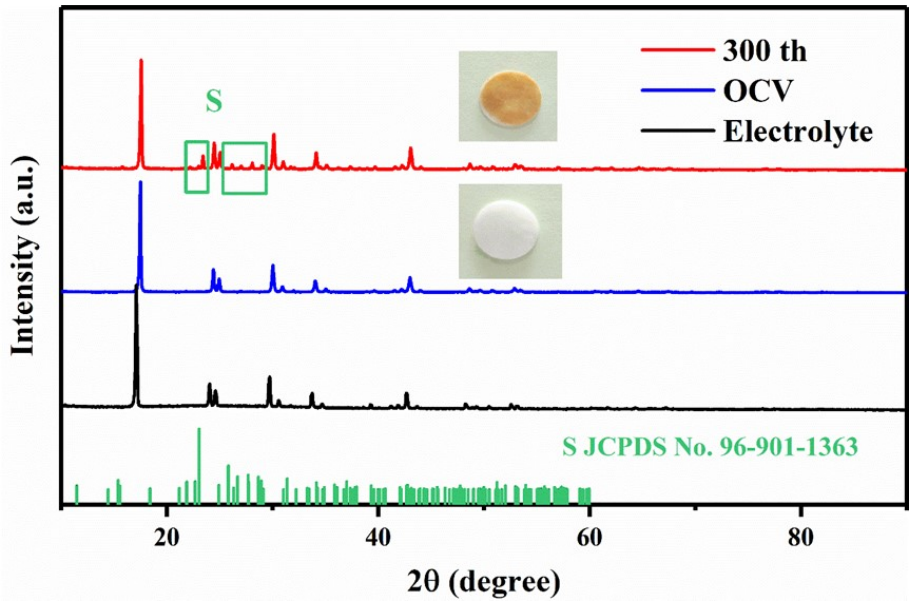

Fig. S30. The XRD patterns of the separator at the OCV state and yellow separator after 300 cycles.

In order to determine what the yellow material on the surface of the separator after cycling, we performed the EDS (Fig. S29) and XRD (Fig. S30) characterizations of the yellow separator. As shown in Fig. S29, it can be seen that there is a significant presence of S in addition to the elements of the separator itself (SiO_2, Al_2O_3), so it can be preliminarily judged that the yellow substance on the separator is the S element. Subsequently, we carried out the XRD characterization (Fig. S30) of the separator on the OCV state and after cycling 300 cycles (yellow separator), and it can be seen that the XRD peaks of the yellow separator compared with the white separator of OCV state, the extra peaks belong to the S element in addition to the peak of the electrolyte, which confirms that the yellow material on the surface of the yellow separator after cycling is the S element.

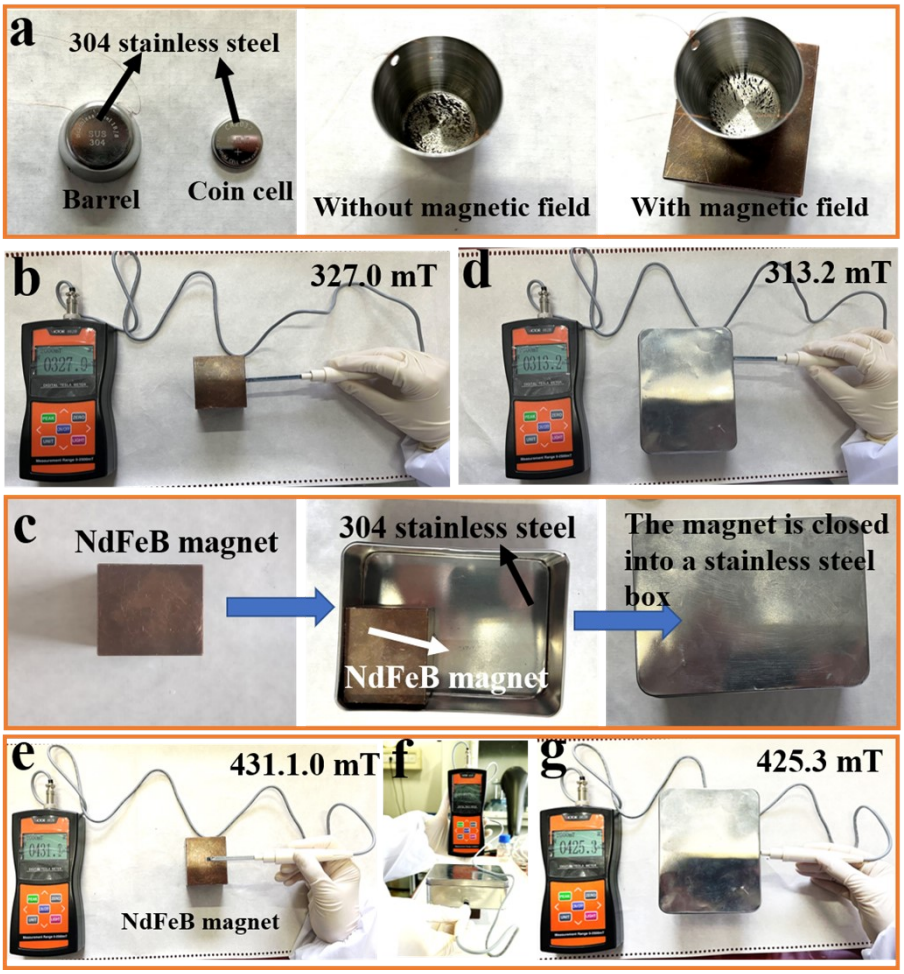

Fig. S31. (a) The state of iron powders in 304-type stainless steel barrel-shape vessel with or without magnetic field. (b) The magnetic field strength on the side of the magnet. (c) The demonstration process that magnet is placed into a 304 stainless steel box. (d) The magnetic field strength on the side of the box (the magnet is closed into the box). (e) The magnetic field strength above the magnet. (f) Placing the stainless steel box above the magnet. (g) The magnetic field strength inside the stainless steel box above the magnet.

To clarify the real magnetic-filed effect in the present coin cell, we supplied some experiments in the revised manuscript: Firstly, to intuitively observe the magnetic field effect inside the coin-type battery, and possibly avoid the influence of leaking magnetic field in an open battery shell, we chose a deeper barrel-shape vessel and some iron powders were put on the inside of the vessel. The material of the vessel is also the 304-type stainless steel, which is the same with coin-type battery. We can find that the iron powders are flat and scattered at the bottom of the vessel without magnetic field, and become upright with magnetic field from the magnet as shown in Fig. S31a and

Supplementary Video S3. The result shows that the deeper barrel-shape vessel has weak magnetic shielding effect. Secondly, considering that the barrel-shape vessel is still an open environment, which is not exactly the same with that of the coin-type battery (Fig. S31a). So, two other experiments were done to simulate the real magnetic environment inside the battery, where we put the magnet into a 304-type stainless steel box (Fig. S31c) and measured the lateral magnetic field strength with and without the enclosed box via a magnetometer device. The results show that the values of the lateral magnetic field strength almost the same with/without the enclosed box as shown in the Fig. S31b and d, and Supplementary Video S4. Moreover, to more realistically simulate magnetic field effect on inside battery environment, we further cut a very small hole on the side of the enclosed box, and then put it on the top of the magnet shown in Fig. S31f. Next, we tested the top magnetic field strength under inside/without the box by the magnetometer device as shown in Fig. S31e-g, and Supplementary Video S5. The results also present that the values of the top magnetic field strength almost the same with/without the enclosed box at the top. That is to say, the 304-type stainless steel box has little impact on the magnetic field effect.

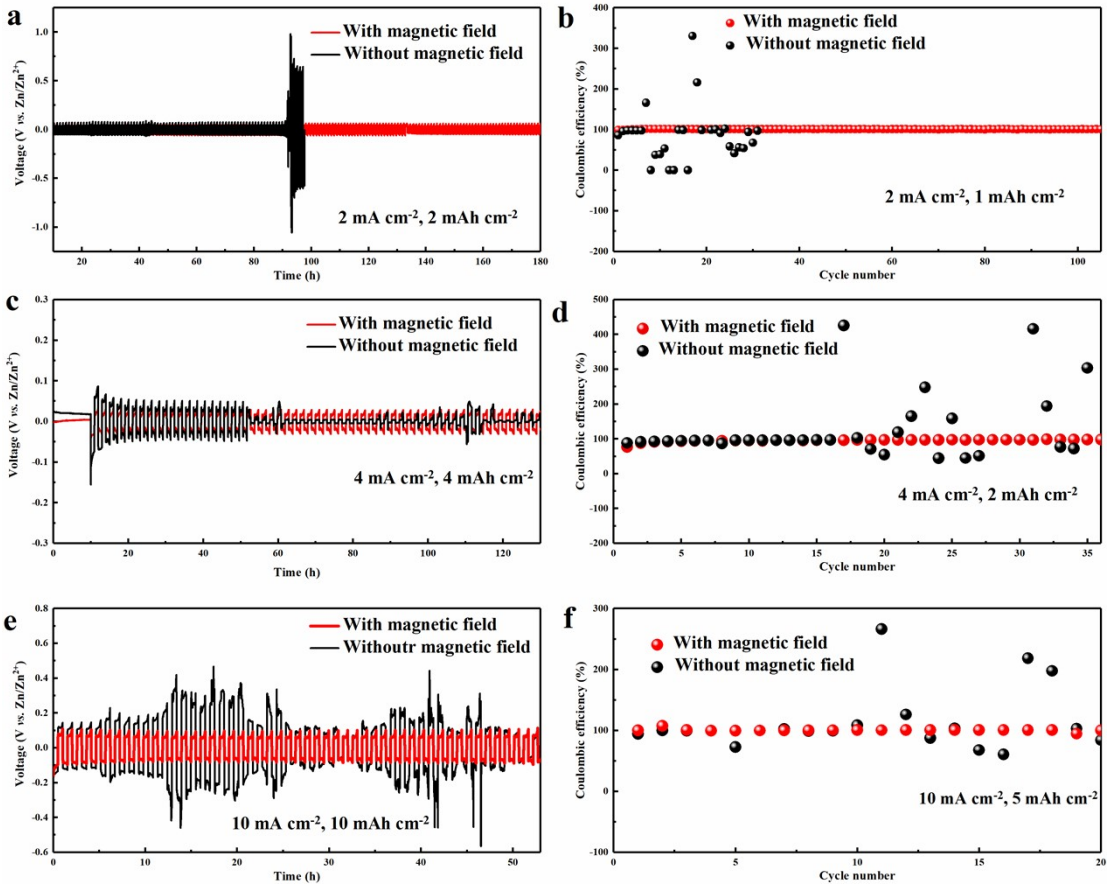

Fig. S32. The electrochemical performance of Zn||Zn and Zn||Cu cells under 2 mA cm^{-2} (a, b), 4 mA cm^2 (c,d) and 10 mA cm^{-2} (e,f).

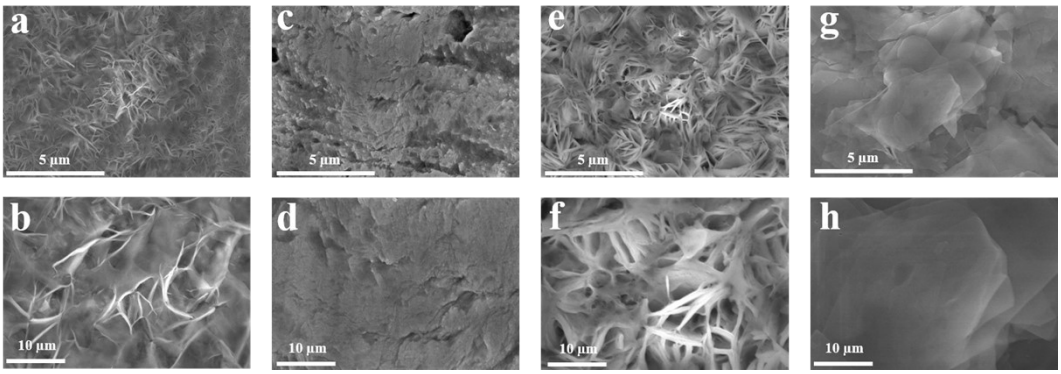

Fig. S33. (a-d) SEM images of the cycled Zn anode surface of the Zn||Zn batteries without magnetic field (a,b), and with magnetic field (c,d). (e-h) SEM images of the cycled Cu surface of the Zn||Cu batteries without magnetic field (e,f), and with magnetic field (g,h).

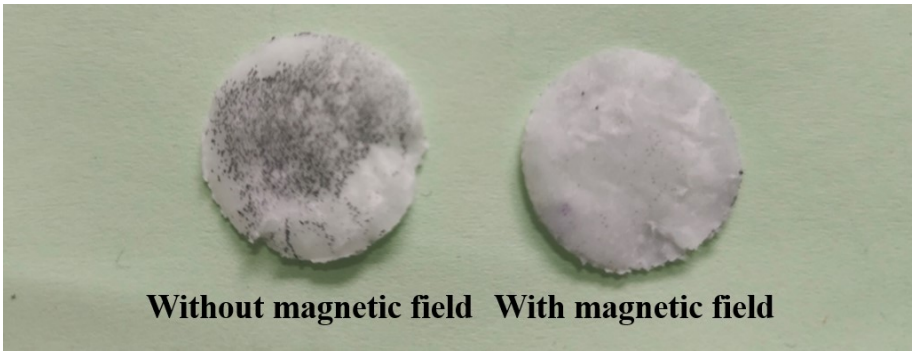

Fig. S34. The digital photo of the separator with or without magnetic field.

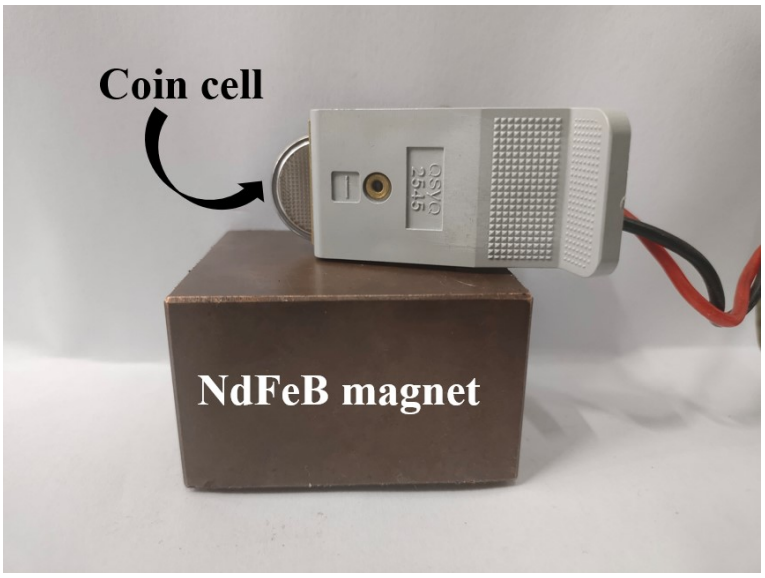

Fig. S35. The digital photo of the experimental setup of the coin cell under magnetic field.

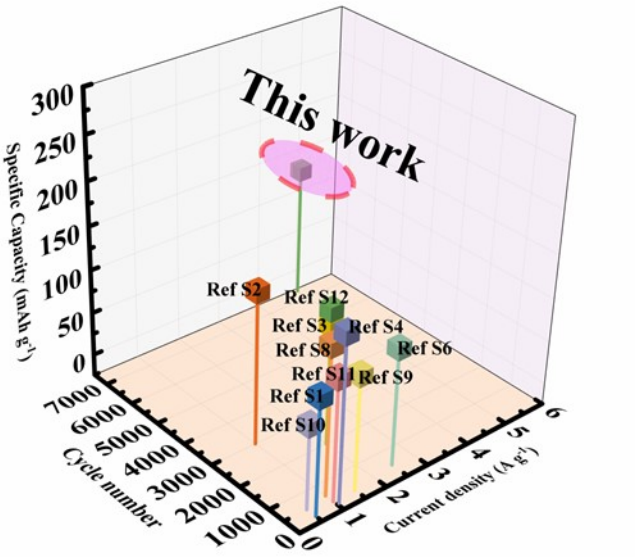

Fig. S36. The cycling performance comparison of the VS_2||Zn AZIB with the previously reported works.

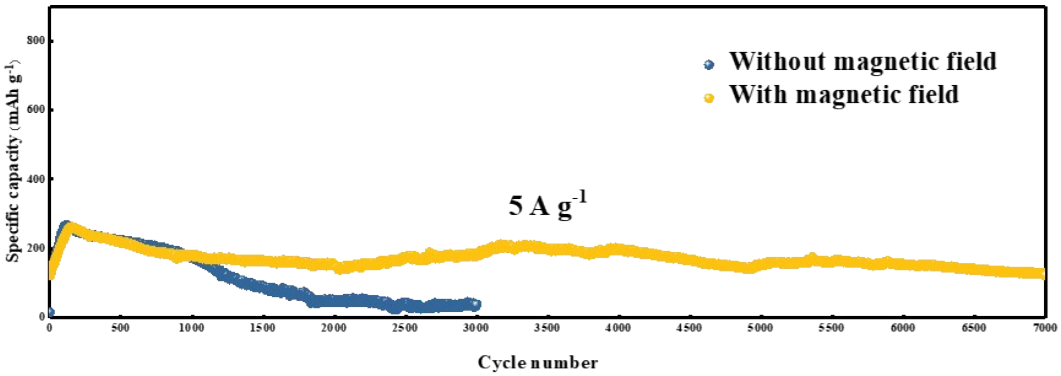

Fig. S37. The cycling performance comparison of the Zn-VS_2 batteries with or without magnetic field.

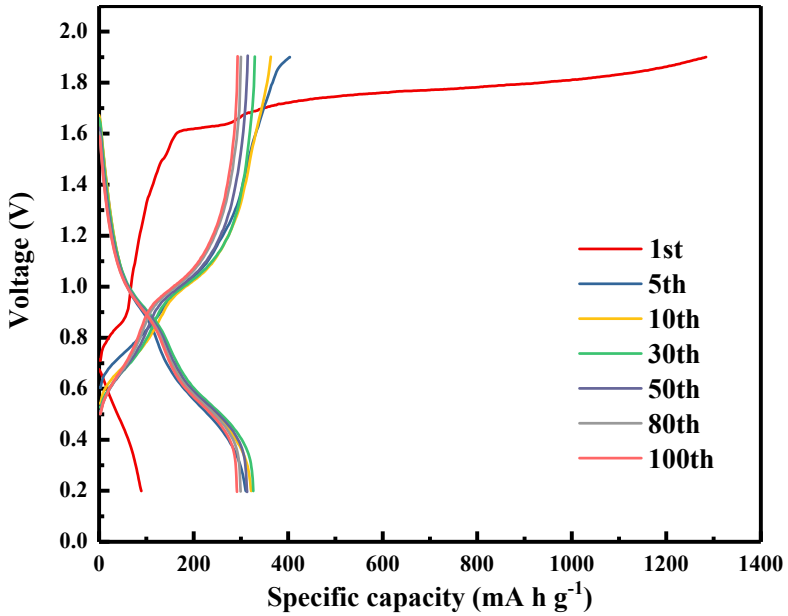

Fig. S38. The first 100 cycles cycling voltage profiles of the Zn-VS_2 AZIB at 1 A g^{-1}.

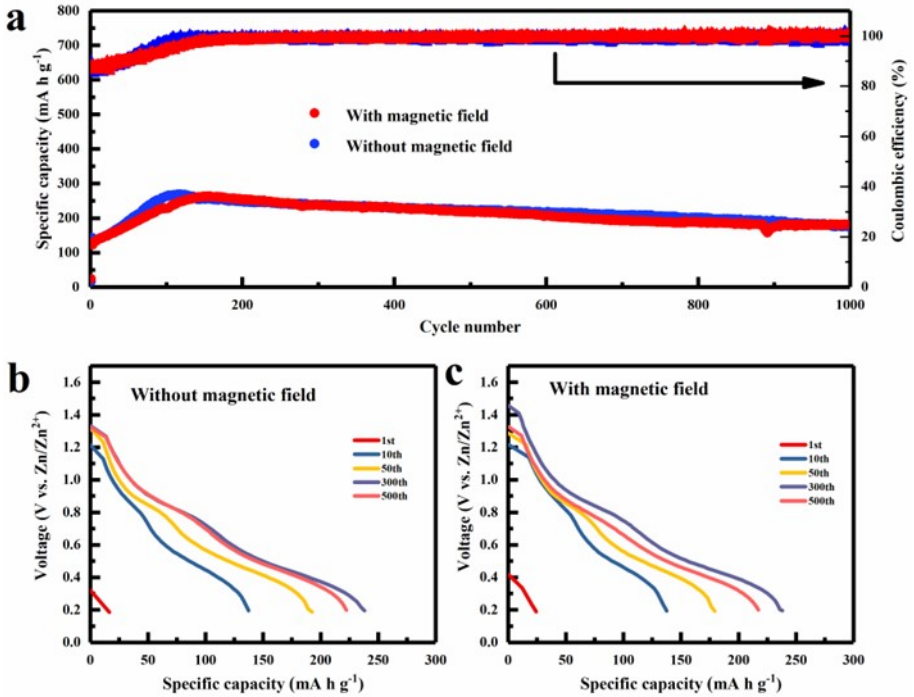

Fig. S39. (a) Discharge capacity comparison of the VS_2 cathode with or without magnetic field. The galvanostatic discharge curves of the VS_2 cathode at different cycle (b) without magnetic field and (c) with magnetic field.

As we know, the intercalation process of zinc ions in a cathode material can be intuitively reflected by the discharge capacity from the galvanostatic discharge curve. We found that the cycling performance of the VS_2 cathode decreased sharply after 1,200 cycles without magnetic field due to the corrosion of the zinc metal and the growth of zinc dendrites. Based on the above results, we compared the discharge capacities (Fig. S39a) and discharge curves (Fig. S39b and c) of the first 1,000 cycles with or without magnetic field. Fig. S39a shows the discharge capacity of VS_2 battery with or without magnetic field. It can be seen that the two discharge capacity values are almost the same. Moreover, the discharge curve shapes at different cycle of the VS_2 battery are also almost the same (Fig. S39b and c) with and without the application of magnetic field. So, we infer that the magnetic field only affects the trajectory of zinc ions when they reach the electrode surface, the intercalation and transport of zinc ions within the cathode material may not be affected.

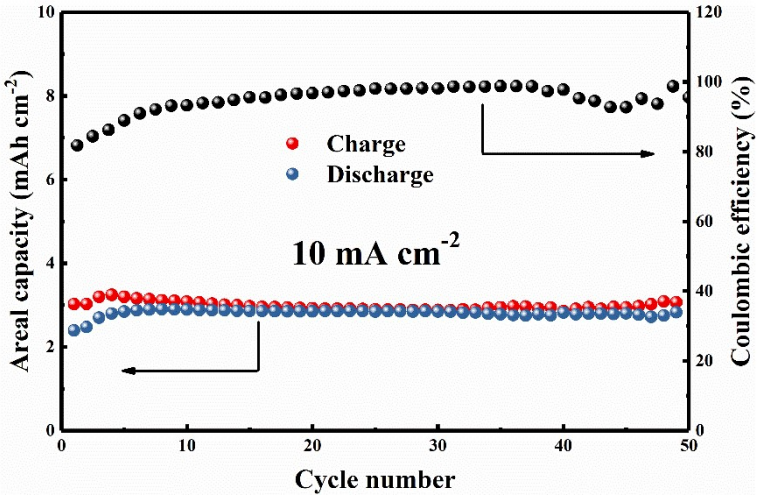

Fig. S40. The areal specific capacity of the Zn-VS_2 battery at 10 mA cm^{-2}.

Supplementary References

[S1] P. He, M. Yan, G. Zhang, R. Sun, L. Chen, Q. An and L. Mai, Adv. Energy Mater., 2017, 7 1601920.

[S2] D. Yu, Z. Wei, X. Zhang, Y. Zeng, C. Wang, G. Chen, Z. X. Shen and F. Du, Adv. Funct. Mater., 2020, 31, 2008743.

[S3] T. Jiao, Q. Yang, S. Wu, Z. Wang, D. Chen, D. Shen, B. Liu, J. Cheng, H. Li, L. Ma, C. Zhi and W. Zhang, J. Mater. Chem. A, 2019, 7, 16330-16338.

[S4] H. Qin, Z. Yang, L. Chen, X. Chen and L. Wang, J. Mater. Chem. A, 2019, 6, 23757-23765.

[S5] B. S. Yin, S. W. Zhang, T. Xiong, W. Shi, K. Ke, W. S. V. Lee, J. Xue and Z. B. Wang, New J. Chem., 2020, 44, 15951-15957.

[S6] Q. Zhu, Q. Xiao, B. Zhang, Z. Yan, X. Liu, S. Chen, Z. Ren and Y. Yu, J. Mater. Chem. A, 2020, 8, 10761-10766.

[S7] T. Chen, X. Zhu, X. Chen, Q. Zhang, Y. Li, W. Peng, F. Zhang and X. Fan, J. Power Sources, 2020, 477, 228652.

[S8] J. Liu, W. Peng, Y. Li, F. Zhang and X. Fan, J. Mater. Chem. C, 2021, 9, 6308-6315.

[S9] X. Pu, T. Song, L. Tang, Y. Tao, T. Cao, Q. Xu, H. Liu, Y. Wang and Y. Xia, J. Power Sources, 2019, 437, 226917.

[S10] Z. Wu, C. Lu, Y. Wang, L. Zhang, L. Jiang, W. Tian, C. Cai, Q. Gu, Z. Sun and L. Hu, Small, 2020, 16, e2000698.

[S11] J. Zhu, T. Jian, Y. Wu, W. Ma, Y. Lu, L. Sun, F. Meng, B. Wang, F. Cai, J. Gao, G. Li, L. Yang, X. Yan and C. Xu, Appl. Surf. Sci., 2021, 544, 148882.

[S12] Y. Tan, S. Li, X. Zhao, Y. Wang, Q. Shen, X. Qu, Y. Liu and L. Jiao, Adv. Energy Mater., 2022, 12, 2104001.